Editors' Suggestion

All-electrical cooling of an optically levitated nanoparticle

Oscar Kremer,[1] Igor Califrer,[2] Daniel Tandeitnik,[2] Jean Pierre von der Weid,[1]
Guilherme Temporão,[1] and Thiago Guerreiro[2,*]

[1] *Department of Electrical Engineering, Pontifical Catholic University of Rio de Janeiro, Rio de Janeiro, RJ 22451-900, Brazil*
[2] *Department of Physics, Pontifical Catholic University of Rio de Janeiro, Rio de Janeiro 22451-900, Brazil*

(Received 8 March 2024; revised 30 May 2024; accepted 28 June 2024; published 5 August 2024)

We implement an all-electrical controller for 3D feedback cooling of an optically levitated nanoparticle capable of reaching subkelvin temperatures for the center-of-mass motion. The controller is based on an optimal policy in which state estimation is made by delayed position measurements. The method offers a simplified path for precooling and decoupling the transverse degrees of freedom of the nanoparticle. Numerical simulations show that in an improved setup with quantum limited detection, all three axes can be cooled down to a few-phonon regime.

DOI: 10.1103/PhysRevApplied.22.024010

I. INTRODUCTION

Optical tweezers [1] have emerged as a valuable tool for isolating and controlling the motion of micro- and nano-objects [2–4]. Through clever combinations with electric and magnetic traps and actuators [5–9], optical traps can be used to create highly sensitive sensors for force, acceleration, and torque [10–14], and such a high degree of control enables cooling of the center-of-mass (CoM) motion of a levitated nanoparticle to the ground state [15–18]. Moreover, optical tweezers provide a versatile platform for many-body [19–23] and fundamental physics experiments, with applications in diverse areas such as stochastic thermodynamics [24–28], nonlinear dynamics [27,29–32], the search for new particles and forces of nature [33–38], and unprecedented tests of quantum mechanics [39–43]. All these applications require the levitated object to be well isolated from its surrounding environment, and this isolation is mainly limited by the vacuum quality during the experiment, photon-recoil heating [44], and black-body radiation [45]. Regarding the vacuum quality, since the nano-object is initially trapped at atmospheric pressure, it is thermalized at room temperature, preventing stable trapping at low pressures and rendering the trapping potential nonlinear due to large thermal fluctuations [29]; therefore, cooling the object's motion is often a prerequisite for levitation experiments.

Active feedback cooling [46,47], in particular parametric cooling, has emerged as the standard technique for achieving 3D cooling of a levitated nanoparticle's motion [48], enabling temperatures as low as the submillikelvin range [44]. In practice, parametric control techniques are often used as a precooling mechanism. The performance of parametric feedback, however, comes at the cost of employing a nonlinear control protocol, which modulates a portion of the optical-trapping power according to the resonance frequencies of the nanoparticle. In addition, expensive electro- or acousto-optic modulators must be used in combination with lock-in devices capable of modulating a signal locked to the particle's motion. Alongside the parametric control, once the thermal occupation number has been reduced to around 10^3, the levitated object's charge can be exploited to further control its motion along one direction to even lower temperatures, all the way into the quantum ground state [17,18].

In this letter, we explore an all-electrical approach to precooling the motion of a levitated nanoparticle from room temperature to a point at which the trap's nonlinear features are significantly reduced and stable trapping can be achieved in high vacuum ($p < 10^{-3}$ mbar). To do so, we design a simple electric actuator based on a custom-made printed circuit board (PCB) that is capable of influencing the particle's motion via Coulomb forces. Fine alignment of the PCB with the levitated nanoparticle is not required. After a careful calibration of the electrical forces, we employ a delayed-feedback scheme to 3D cool the CoM motion of the particle. We experimentally measure the effect of the delay in the feedback force and show excellent agreement with theoretical predictions [49]. Finally, in a first step toward the larger effort of simplifying optomechanical cooling experiments, we successfully demonstrate 3D cooling down to subkelvin temperatures while completely avoiding modulation of the trap's power. With numerical simulations based on our

*Contact author: barbosa@puc-rio.br

electrical actuator, we argue that, when combined with a stiffer optical trap, quantum limited detection for all three axes [50], and optimal quantum state estimation [51–53], an all-electrical optimal control approach can be employed to reach a few-phonon regime in all three axes.

We highlight that 3D electrical feedback cooling of levitated nanoparticles has been recently implemented in levitated optomechanics experiments—see Refs. [54–56] for examples using integrated chip photonics, a hybrid optical Paul trap, and finely aligned electrode tips. Our setup adds a simplified solution to that list while still offering the possibility of 3D quantum control of a levitated nanoparticle. The remainder of this paper is organized as follows. In Sec. II, we briefly describe the equations of motion and the linear quadratic regulator (LQR), which is used to evaluate the optimal proportional and derivative gains used in the control feedback. Next, Sec. III describes the experimental setup, while Sec. IV shows the results of all-electrical feedback cooling experiments and the prospects for 3D ground-state cooling. We conclude in Sec. V with a brief discussion.

II. THEORY

The CoM motion along the x, y, and z axes of an optically levitated nanoparticle trapped by a strongly focused Gaussian beam can be effectively modeled through a set of second-order Langevin equations,

$$\ddot{x}(t) + \gamma_m \dot{x}(t) + \Omega_x^2 x(t) = \frac{1}{m} F_{\text{th},x}(t) + b_x u_x, \quad \text{(1a)}$$

$$\ddot{y}(t) + \gamma_m \dot{y}(t) + \Omega_y^2 y(t) = \frac{1}{m} F_{\text{th},y}(t) + b_y u_y, \quad \text{(1b)}$$

$$\ddot{z}(t) + \gamma_m \dot{z}(t) + \Omega_z^2 z(t) = \frac{1}{m} F_{\text{th},z}(t) + b_z u_z, \quad \text{(1c)}$$

where m is the particle's mass, γ_m is the drag coefficient, Ω_i is the angular frequency along the i axis, and $F_{\text{th},i}$ represents the (white-noise) stochastic force on each axis due to residual gas pressure in the vacuum chamber, satisfying

$$\langle F_{\text{th},i}(t)\rangle = 0, \quad \text{(2a)}$$

$$\langle F_{\text{th},i}(t) F_{\text{th},j}(t+\tau)\rangle = 2m\gamma_m k_B T \delta_{ij}\, \delta(\tau), \quad \text{(2b)}$$

where k_B is the Boltzmann constant, T is the residual gas temperature, δ_{ij} is the Kronecker delta, and $i,j \in \{x, y, z\}$. The $b_i u_i$ terms in Eqs. (1) account for external forces that may influence the particle's motion, with u_i representing the control signals defining feedback forces acting on the trapped particle.

By defining the state vector

$$\mathbf{x}(t) \equiv \begin{bmatrix} x(t) & y(t) & z(t) & \dot{x}(t) & \dot{y}(t) & \dot{z}(t) \end{bmatrix}^T, \quad (3)$$

one can then write Eqs. (1) in the state-variable representation [57], resulting in the multiple-input-multiple-output system

$$\dot{\mathbf{x}}(t) = \mathbf{A}\mathbf{x}(t) + \mathbf{B}\mathbf{u}(t) + \mathbf{w}(t), \quad (4)$$

where

$$\mathbf{A} = \begin{bmatrix} \mathbf{0}_{3\times 3} & \mathbf{I}_3 \\ -\text{diag}(\Omega^2) & -\gamma_m \mathbf{I}_3 \end{bmatrix}, \quad \mathbf{w}(t) = \frac{1}{m}\begin{bmatrix} \mathbf{0}_{3\times 1} \\ \mathbf{F}_{\text{th}}(t) \end{bmatrix}, \quad (5)$$

and

$$\mathbf{B} = \begin{bmatrix} \mathbf{0}_{3\times 3} \\ \text{diag}(b_x, b_y, b_z) \end{bmatrix}, \quad \mathbf{u} = \begin{bmatrix} u_x \\ u_y \\ u_z \end{bmatrix}, \quad (6)$$

with

$$\Omega^2 = \begin{bmatrix} \Omega_x^2 & \Omega_y^2 & \Omega_z^2 \end{bmatrix}^T$$

and

$$\mathbf{F}_{\text{th}}(t) = \begin{bmatrix} F_{\text{th,x}}(t) & F_{\text{th,y}}(t) & F_{\text{th,z}}(t) \end{bmatrix}^T.$$

Note that due to the geometry of the feedback actuators in our experiment, the submatrix in $\mathbf{B}$ is not block diagonal but assumes a more complicated form; see Sec. III for more details.

Optimal control theory provides tools to find a control policy $\mathbf{u}(t)$ capable of minimizing the energy of a physical system. For linear systems, such as the one described by Eq. (4), this is achieved by the LQR, a controller in which the optimization task targets the minimization of a quadratic cost criterion J of the form

$$J = \frac{1}{2}\int_0^\infty [\mathbf{x}^T(t)\mathbf{Q}\mathbf{x}(t) + \mathbf{u}^T(t)\mathbf{R}\mathbf{u}(t)]\, dt, \quad (7)$$

where $\mathbf{Q}$ is a weighting matrix and $\mathbf{R}$ is a control-effort matrix. The optimal control policy that minimizes Eq.(7) is [58]

$$\mathbf{u} = -\mathbf{K}\mathbf{x}, \quad (8)$$

where $\mathbf{K} = \mathbf{R}^{-1}\mathbf{B}\mathbf{S}$ is the controller's gain matrix and $\mathbf{S}$ is the solution of the algebraic Riccati equation

$$\mathbf{S}\mathbf{A} + \mathbf{A}^T\mathbf{S} + \mathbf{Q} - \mathbf{S}\mathbf{B}\mathbf{R}^{-1}\mathbf{B}^T\mathbf{S} = \mathbf{0}. \quad (9)$$

Practical application of the LQR poses the significant challenge of obtaining the complete state vector $\mathbf{x}$. Experimentally, access is not granted to $\mathbf{x}$ but rather to a measurement vector $\mathbf{y}$, which is related to the states according to

$$\mathbf{y}(t) = \mathbf{C}\mathbf{x}(t) + \mathbf{m}(t), \quad (10)$$

where $\mathbf{C}$ is a 3×6 matrix, known as the output matrix (see Appendix C for more details about its structure). The term $\mathbf{m}$ is the measurement-noise vector, which can be expressed

$$\mathbf{m} = \begin{bmatrix} \zeta_x(t) & \zeta_y(t) & \zeta_z(t) \end{bmatrix}^T.$$

Here, $\zeta_i(t)$ are zero-mean white-noise processes with variance σ_i^2, satisfying

$$\langle \zeta_i(t) \rangle = 0, \tag{11a}$$

$$\langle \zeta_i(t)\zeta_j(t+\tau) \rangle = \sigma_i^2 \delta_{ij}\delta(\tau). \tag{11b}$$

Measurements of $x(t)$, $y(t)$, and $z(t)$ can be implemented by collecting forward- or backward-scattered light from the nanoparticle [50]; however, the velocities are not accessible experimentally. An optimal estimation $\hat{\mathbf{x}}$ can be computed by applying real-time filtering techniques to estimate $\mathbf{x}$. For linear dynamics in which the disturbances and measurement noise adhere to Eqs. (2) and (11), $\mathbf{x}$ is best estimated using a Kalman filter [59,60].

Implementing the Kalman filter significantly increases the complexity of the feedback loop. As a simplification, it is possible to estimate the velocity as being proportional to a delayed position measurement. This approach has proven successful for cooling one of the spatial degrees of freedom of a levitated nanoparticle [46], albeit increasing the minimal effective temperature achievable. The effective temperature for each axis can be computed by using the integral [18]

$$T_{\text{eff}}^i = \frac{m\Omega_i^2}{k_B}\int_0^\infty \left(1 + \frac{\Omega^2}{\Omega_i^2}\right) S_{ii}(\Omega)\, d\Omega - \frac{1}{2}, \tag{12}$$

where S_{ii} is the double-sided power spectral density (PSD) for the particle's motion along the i axis, expressed as

$$S_{ii} = \frac{2\gamma_m k_B T}{m[(\Omega^2 - \Omega_i^2)^2 + \gamma_m^2 \Omega_i^2]}. \tag{13}$$

Note that the PSD is computed directly from measurements of the particle's position.

III. EXPERIMENT

The experimental setup is schematically illustrated in Fig. 1(a). A cw laser at 1550 nm (RIO Orion) amplified by an erbium-doped fiber amplifier (Keopsys CEFA-C-BO-HP-SM) is used to produce a high-quality Gaussian beam linearly polarized along the x direction with a power of $P_t \approx 2$ W at the output of a single-mode fiber. The beam is focused by an aspheric lens (Thorlabs C330TM-C, NA = 0.68) assembled inside a vacuum chamber, allowing for stable optical trapping. The light scattered by the particle along the forward direction is collimated by a collecting lens (Thorlabs C110TM-C, NA = 0.40). Silica nanoparticles (diameter 143 nm, microParticles GmbH) are loaded into the vacuum chamber using a nebulizer and trapped at atmospheric pressure. The trapped particle oscillates with resonance frequencies along the three axes given by $\Omega_x/2\pi = 96.24$ kHz, $\Omega_y/2\pi = 101.49$ kHz, and $\Omega_z/2\pi = 31.52$ kHz.

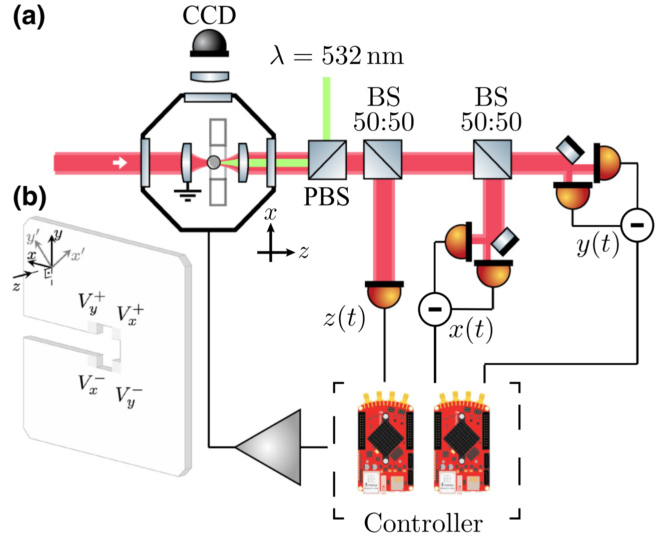

FIG. 1. Experimental setup. (a) Simplified scheme of the setup. An optical tweezer is assembled within a vacuum chamber, and a CCD is used for imaging of the tweezed particle upon illumination with a 532-nm laser beam. The trapping lens is grounded, and detection of forward-scattered light is used to generate the electrical-feedback signal sent to the electrodes. The collection lens works as the z electrode, whilst the board shown in (b) is placed close to the trap's focus and contains the x and y electrodes. The axes at the top left indicate the orientation between the electrodes' axes (x', y') and the coordinate system of the detection. We note that, along with an appropriate choice of design parameters, sufficient proximity between the center of the PCB and the tweezer focus ensure that the beam is not cropped by the board.

Detection of transverse motion, $x(t)$ and $y(t)$, is carried out using balanced photodiodes (Newport 2117-FC), while information about the longitudinal $[z(t)]$ direction is obtained by direct intensity photodetection. The optical trap is characterized through measurements of the particle's position PSDs for each direction. Information on the occupation numbers and effective temperatures of each direction can also be obtained from the PSDs by using Eq. (12).

A PCB containing two orthogonal pairs of electrodes, as illustrated in Fig. 1(b), is placed in the vicinity of the optical trap's focus, allowing for two-dimensional electrical feedback control of the nanoparticle's CoM motion. The PCB has a thickness of 1.5 mm and is designed to be compatible with cage plate optical systems (Thorlabs SP02). The four square-shaped contacts (2×2 mm^2) around its center are arranged symmetrically, with a separation of 2.5 mm between adjacent contacts. Note also that only coarse alignment of the PCB with respect to the levitated nanoparticle is required, and this can be achieved by placing the PCB near the optical focus. Due to the control method employed, coupling between degrees of freedom in the transverse plane is compensated by the calibration process.

A third pair of electrodes is implemented by applying an electric signal to the mount of the collection lens, producing a voltage difference with respect to the grounded trapping lens. Simulations conducted using the finite-element method have numerically demonstrated that this voltage difference establishes a uniform electric field near the particle's position [31]. The signal from the detection is digitally processed by two FPGAs (STEMlab 125-14, Red Pitaya) and analog amplified before being fed back to the electrodes. We remove any crosstalk between the z and xy electrodes by digital filtering, which is facilitated by the difference in characteristic frequencies between the longitudinal and transverse degrees of freedom. Taking this and the geometry of the actuators into consideration, the gain matrix assumes a block diagonal form,

$$\mathbf{K} = \begin{bmatrix} \mathbf{K}_{p,xy} & 0 & \mathbf{K}_{d,xy} & 0 \\ \mathbf{0}_{1\times 2} & k_{p,z} & \mathbf{0}_{1\times 2} & k_{d,z} \end{bmatrix}. \tag{14}$$

A detailed description of the analog amplification and the digital processing of the detection signal can be found in Appendix B. Digital processing includes frequency filtering, delaying, and application of derivative/proportional gains to the signal. The choice of optimal gains was based on control theory, as presented in Appendix A. Since the theory predicts only a weak dependence of optimal gain on pressure, we consider a single gain to be optimal throughout the experiment.

Appropriate calibration of the electrodes accounts for misalignment between their axes and the mechanical modes, allowing for a partial reconstruction of the **B** matrix, which assumes a 45°-rotated form with respect to the diagonal matrix given by Eqs. (1). During calibration, the effect of the z electrode was observed to be too weak, meaning that only the x and y electrodes could be calibrated. This led to the control LQR being applied only to the x and y motion and a cold damping protocol [18,47] being applied along the z direction ($k_{p,z} = 0$). We refer the reader to Appendix C for more information on the calibration procedure.

IV. RESULTS

Proper implementation of the control method as described above requires precisely delaying each detection signal. The delay characterization process involves applying forces proportional to the delayed position independently in the x and y directions. For instance, referring to Eq. (1), this translates to $u_x = G_x x(t - \tau_x)$ for the x coordinate (and similarly for y and z). Each delay τ_i consists

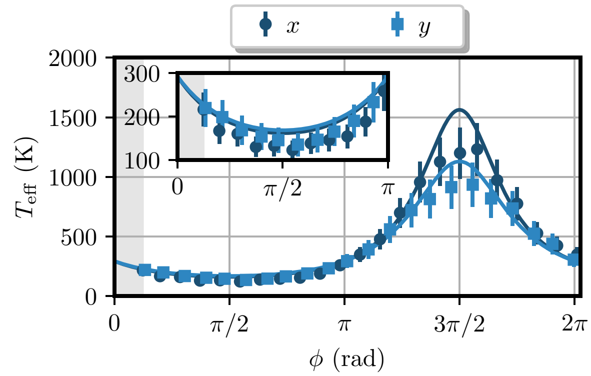

FIG. 2. Effect of delayed-feedback forces. A comparison between experimental results and theory (solid lines) is presented. Measurements were conducted at room temperature (293 K) and a pressure of 1.2 mbar. Each data point corresponds to ten thousand 50-ms traces. The gains used were $G_x = (9.17 \pm 0.98) \times 10^{-9}$ N/m and $G_y = (8.97 \pm 0.97) \times 10^{-9}$ N/m. The gray shaded area marks the region that could not be measured due to the minimal delay imposed by the electronics. The horizontal axis, ϕ, represents the phase $\Omega_i \tau_i$ introduced by the delay. In the inset, the interval during which the delay induces cooling is presented in more detail.

of two components, the intrinsic electronic delay $\tau_{e,i}$ and an adjustable delay $\tau_{c,i}$. Figure 2 shows measures of $T^x_{\rm eff}$ and $T^y_{\rm eff}$ while subjecting the particle to the delayed force. The controllable delay $\tau_{c,i}$ was varied to span the range of τ_i from $\tau_{e,i}$ to one period of oscillation ($\phi = 2\pi$). The experimental results show excellent agreement with the theoretical predictions from Ref. [49]. Furthermore, this measurement allowed for the characterization of the electronic delays, $\tau_{e,x}$ and $\tau_{e,y}$, both of which were determined to be 0.639 µs. We assume that $\tau_{e,z}$ has the same value.

Figure 3(a) shows the results of 3D feedback cooling. The minimal effective temperatures achieved in the experiment are $T^x_{\rm eff} = (0.58 \pm 0.12)$ K, $T^y_{\rm eff} = (0.55 \pm 0.11)$ K, and $T^z_{\rm eff} = (3.63 \pm 0.77)$ K, for each of the three axes. The gray shaded area in Fig. 3(a) depicts an instability region observed near 10^{-2} mbar, which is characterized by a sudden increase in $T^i_{\rm eff}$. We attribute this phenomenon to variations on the net charge of the nanoparticle [61]. The net charge acts as a linear parameter affecting the input matrix, thus linearly impacting the control gain. As electrode calibration was performed at high pressure (>1 mbar), for pressures less than 0.01 mbar, it cannot be assumed that the applied gain was optimal. Nonetheless, stable cooling has been implemented by using only electrical actuators, and the application of LQR returned a gain matrix capable of handling any coupling between degrees of freedom in the dynamics. The PSD of the CoM motion for the y direction under three distinct pressures is shown in Fig. 3(b). Feedback cooling not only reduces the area of the PSD, from which the effective temperatures are estimated, but it also introduces a term that increases its linewidth, as

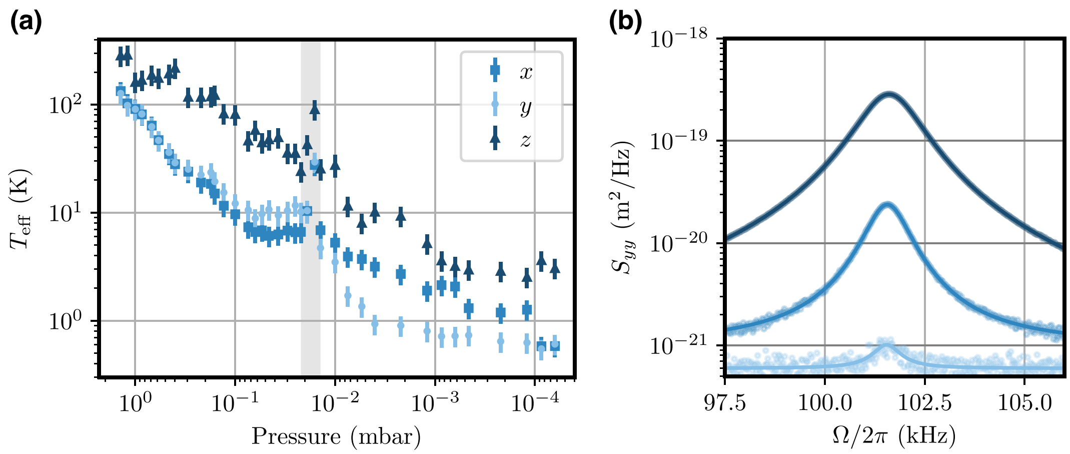

FIG. 3. All-electrical cooling. (a) Dependence of x, y, and z effective temperatures on pressure, calculated using Eq. (12). The gray shaded region shows a region of instability, as discussed in the main text. (b) PSD of the y motion. Measurements were made at 1.0 mbar (—), 5.4×10^{-2} mbar (—), and 1.2×10^{-4} mbar (—).

expected due to the presence of derivative terms in the nanoparticle's motion.

For pressures less than 0.01 mbar, no instability has been encountered, agreeing with results previously observed [62]; therefore, the control protocol employed should be capable of successfully controlling the nanoparticle until the stochastic thermal force becomes negligible and the dynamics start to be dominated by measurement backaction and photon-recoil heating. When compared to parametric cooling, an all-electrical approach is advantageous because it avoids contamination of the signal by spurious modulation signals, which are rendered unnecessary. Additionally, in contrast to parametric cooling, the LQR employs a linear control law, and it thus does not affect the overall linearity of the system.

Since the LQR has been successfully employed in combination with a Kalman filter for ground-state cooling along the longitudinal axis [17], extending its application as a 3D quantum control policy should be experimentally achievable. By considering the electrode parameters presented in Appendix C, an implementation of a Kalman filter for state estimation, and the trapping and detection-efficiency parameters reported in [17], we numerically simulated 3D all-electrical cooling of a trapped nanoparticle. Figure 4 presents the expected final mean occupation numbers with our all-electrical controller. To account for quantum effects, the same parameters of measurement uncertainty, detection efficiency η_z, and backaction provided in Ref. [17] were taken into account in the simulation. Note that the simulation considers a backward detection scheme, resulting in a higher detection efficiency for the longitudinal axis compared to the transverse axes, thereby leading to a smaller thermal occupancy for z. In contrast, the experiment employed a forward detection scheme, therefore yielding the opposite effect due to limited detection efficiency [50]. The detection efficiency along the transverse axes, η_x and η_y, were computed by considering the expected proportion between the efficiency along x and y and the longitudinal directions for the corresponding trap's NA [50]. Such efficiencies led to detection imprecisions of 1.561×10^{-20}, 3.122×10^{-20}, and 5.204×10^{-21} m^2/Hz for x, y, and z, respectively. For pressures of the order of , the simulation results agree with the experimental findings in Ref. [17]. It must be noted that, for higher pressures, we expect that experimental imperfections will increase the minimum number of phonons. Moreover, while it is evident that in the simulation, the thermal occupancy for y exceeds that for x, the experimental results in Fig. 3(a) show the opposite. This most likely arises from experimental imperfections due

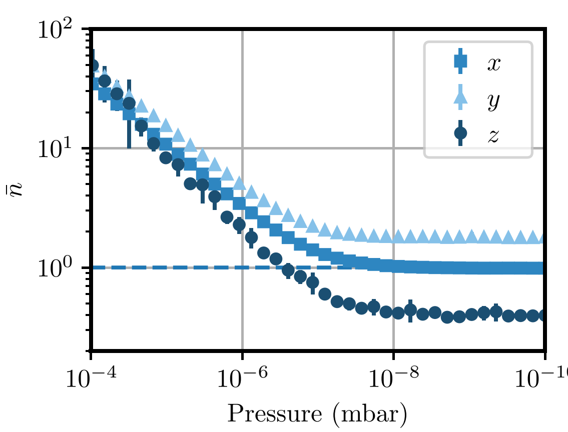

FIG. 4. Simulation of optimal all-electrical 3D cooling with improved trapping lens and detection scheme: expected thermal occupation numbers $\bar{n}$, as obtained from the estimation of the particle's covariance matrix, as a function of pressure for the x, y, and z directions. The dashed line marks a single phonon. The error bars correspond to one standard deviation over 30 simulation runs.

to detection efficiency in the x axis. Note that systematic errors in the experiment—such as errors in the nanoparticle's mass, density, and charge, or imperfections in the calibration processes—will alter the calculation of optimal gain and, consequently, the performance of the cooling protocol.

V. CONCLUSIONS

In conclusion, we have demonstrated an all-electrical feedback cooling scheme for reducing the CoM temperature of a levitated nanoparticle in high vacuum. Through a simple custom-designed electrical actuator, we have shown subkelvin temperatures for the transverse directions of motion, avoiding the use of nonlinear feedback cooling schemes such as parametric feedback cooling. This greatly simplifies levitated optomechanics experiments by avoiding the need for modulation of the trapping power. The results of numerical simulations indicate that future improvements over our setup—in particular, implementation of a higher-NA trapping lens and of the optimal backward detection scheme reported in Ref. [17]—should enable all-electrical 3D cooling near the ground state.

ACKNOWLEDGMENTS

We acknowledge Bruno Melo and Felipe Almeida for useful discussions. We acknowledge Joanna A. Zielińska and Lukas Novotny for experimental help. T.G. acknowledges the Coordenação de Aperfeiçoamento de Pessoal de Nível Superior—Brasil (CAPES)—Finance Code 001, Conselho Nacional de Desenvolvimento Científico e Tecnológico (CNPq), Fundação de Amparo à Pesquisa do Estado do Rio de Janeiro (FAPERJ Scholarship No. E-26/200.252/2023), and Fundação de Amparo à Pesquisa do Estado de São Paulo (FAPESP process No. 2021/06736-5). This work was supported by the Serrapilheira Institute (Grant No. Serra—2211-42299).

APPENDIX A: DIGITAL CONTROL THEORY

In the study and analysis of physical systems, time is conventionally treated as a continuous variable; however, when employing signal processing and control methods, a transition to a discrete representation becomes necessary. This is especially crucial when implementing systems on microprocessors or FPGAs, where a set of instructions is executed based on a sampling frequency f_s [63]. The discrete-time formulation of a state-space model can be obtained through the integral approximation, which is based on the assumption that $\mathbf{x}$ and $\mathbf{u}$ remain constant during a sampling period $T_s = 1/f_s$. The evolution of the system is then considered to unfold at fixed time steps $t_n = nT_s$, leading to the following recursive equations:

$$\mathbf{x}_{n+1} = \mathbf{A}_d\mathbf{x}_n + \mathbf{B}_d\mathbf{u}_n + \bar{\mathbf{w}}_n, \tag{A1a}$$

$$\mathbf{y}_{n+1} = \mathbf{C}_d\mathbf{x}_{n+1} + \bar{\mathbf{m}}_{n+1}, \tag{A1b}$$

where $\mathbf{A}_d$, $\mathbf{B}_d$, and $\mathbf{C}_d$ can be expressed in terms of their continuous analogues,

$$\mathbf{A}_d = \sum_{k=0}^{\infty} \frac{T_s^k}{k!}\mathbf{A}^k, \tag{A2a}$$

$$\mathbf{B}_d = (\mathbf{A}_d - \mathbf{I})\mathbf{A}^{-1}\mathbf{B}, \tag{A2b}$$

$$\mathbf{C}_d = \mathbf{C}. \tag{A2c}$$

Additionally, $\mathbf{x}_n = \mathbf{x}(nT_s)$ and $\mathbf{u}_n = \mathbf{u}(nT_s)$. The discrete disturbance and noise terms, $\bar{\mathbf{w}}_n$ and $\bar{\mathbf{m}}_n$, represent discrete-time white-noise processes adhering to conditions akin to those established in Eqs. (2) and (11) in the main text. Considering

$$\bar{\mathbf{w}}_n = \frac{1}{m}\begin{bmatrix}\mathbf{0}_{3\times 1} & \bar{\mathbf{F}}_{\rm th,n}\end{bmatrix}^T,$$

with

$$\bar{\mathbf{F}}_{\rm th,n} = \begin{bmatrix}\bar{F}_{\rm th,x,n} & \bar{F}_{\rm th,y,n} & \bar{F}_{\rm th,z,n}\end{bmatrix}^T$$

and

$$\bar{\mathbf{m}}_n = \begin{bmatrix}\bar{\zeta}_{x,n} & \bar{\zeta}_{y,n} & \bar{\zeta}_{z,n}\end{bmatrix}^T,$$

the conditions are

$$\langle \bar{F}_{\rm th,i,k}\rangle = 0, \tag{A3a}$$

$$\langle \bar{F}_{\rm th,i,k}F_{\rm th,j,k'}\rangle = 2m\gamma_m k_B T T_s \delta_{ij}\delta_{kk'}, \tag{A3b}$$

and

$$\langle \bar{\zeta}_{i,k}(t)\rangle = 0, \tag{A4a}$$

$$\langle \bar{\zeta}_{i,k}\bar{\zeta}_{j,k'}\rangle = \frac{\sigma_i}{T_s}\delta_{ij}\delta_{kk'}. \tag{A4b}$$

Similar to its continuous version, the LQR for discrete-time systems returns an optimal control law, expressed as a linear combination of the states $\mathbf{x}_n$,

$$\mathbf{u}_n = -\mathbf{K}_d\mathbf{x}_n; \tag{A5}$$

however, the expression for the controller's gain changes to

$$\mathbf{K}_d = (\mathbf{R}_d + \mathbf{B}_d^T\mathbf{S}_d\mathbf{B}_d)^{-1}\mathbf{B}_d^T\mathbf{S}_d\mathbf{A}_d, \tag{A6}$$

where $\mathbf{S}_d$ is the solution of the discrete algebraic Riccati equation

$$\mathbf{S}_d = \mathbf{A}_d^T\mathbf{S}_d\mathbf{A}_d + \mathbf{Q}_d - \mathbf{A}_d^T\mathbf{S}_d\mathbf{B}_d(\mathbf{R}_d + \mathbf{B}_d^T\mathbf{S}_d\mathbf{B}_d)^{-1}\mathbf{B}_d^T\mathbf{S}_d\mathbf{A}_d, \tag{A7}$$

and $\mathbf{Q}_d$ and $\mathbf{R}_d$ are the matrices defining the cost function J_d for the digital control law, which reads

$$J_d = \frac{1}{2}\sum_{n=0}^{\infty}[\mathbf{x}_n^T\mathbf{Q}_d\mathbf{x}_n + \mathbf{u}_n^T\mathbf{R}_d\mathbf{u}_n]. \tag{A8}$$

APPENDIX B: ELECTRONIC SETUP

The control law defined in Eq. (A5) was implemented using two Red Pitayas, each equipped with a Xilinx Zynq 7010 FPGA and a two-channel 14-bit analog-to-digital converter, allowing for a maximum sampling frequency of 125 MHz for two distinct inputs, x_a and x_b. The feedback loop incorporated a decimation block, increasing the sampling time T_s from 8.00 to 64.00 ns, enabling synchronous execution of more complex tasks.

In Fig. 5 a simplified block diagram of the main components implemented within each FPGA is shown. The controller block is responsible for computing the output signal $u_{a,n}$ and $u_{b,n}$, being equivalent to the following expression:

$$\begin{bmatrix} u_{a,n} \\ u_{b,n} \end{bmatrix} = \begin{bmatrix} k^d_{p,aa} & k^d_{p,ab} & k^d_{d,aa} & k^d_{d,ab} \\ k^d_{p,ba} & k^d_{p,bb} & k^d_{d,ba} & k^d_{d,bb} \end{bmatrix} \begin{bmatrix} \tilde{x}_{a,n} \\ \tilde{x}_{b,n} \\ \tilde{x}_{a,n-N_a} \\ \tilde{x}_{b,n-N_b} \end{bmatrix}. \quad \text{(B1)}$$

The signals $\tilde{x}_{a,n}$ and $\tilde{x}_{b,n}$ result from passing the inputs through a dc block and a notch filter, both implemented by using digital biquadratic filters. The constants $k^d_{p,ij}$ and $k^d_{d,ij}$ refer to the digital proportional and derivative gains. The signals $\tilde{x}_{a,n-N_a}$ and $\tilde{x}_{b,n-N_b}$ are the delayed positions, which serve as estimates of the particle's velocity. Here, N_a and N_b are integers representing the applied delay in units of T_s.

The notch-filter transfer function is shown in Fig. 5(b). For the FPGA processing the x and y signals, the transfer function used was H_{xy} to remove harmonic components near Ω_z. In the other FPGA, a filter H_z was applied to remove any components sufficiently close to Ω_x and to Ω_y. The filter's impact on the phase of each signal is approximately constant near each resonance frequency, being included in the overall intrinsic delay of the electronic setup, as discussed in Sec. IV. The computed control signals were sent to noninverting analog amplifiers, providing a constant gain $A = 5.00\,\mathrm{V/V}$ with minimal phase impact for signals with harmonic components from dc up to 150.00 kHz.

APPENDIX C: MODEL PARAMETERS

The implementation of the LQR relies on the accurate extraction of the $\mathbf{A}$ and $\mathbf{B}$ matrices, which are essential for the correct computation of $\mathbf{A}_d$ and $\mathbf{B}_d$. This appendix clarifies how the parameters that allow the reconstruction of these matrices were extracted for the experiment.

1. Detector calibration

Assuming the trapped nanoparticle reaches thermal equilibrium with the residual gas in the vacuum chamber, its initial effective temperature along the three axes is approximately 293 K. Calibration of the detection system involves establishing the linear relationship between the PSD of the detector output for motion along the i axis, denoted as $S_{V_iV_i}(\Omega)$, and the displacement PSD for the same axis, denoted as $S_{ii}(\Omega)$ [64],

$$S_{V_iV_i}(\Omega) = (C^i_{Vm})^2 S_{ii}(\Omega), \quad \text{(C1)}$$

with C^i_{Vm} representing the calibration factor and $S_{V_iV_i}$ being defined by the Lorentzian function,

$$S_{V_iV_i}(\Omega) = (C^i_{Vm})^2 \frac{2\gamma_m k_B T}{m[(\Omega^2 - \Omega_i^2)^2 + \gamma_m^2 \Omega_i^2]}. \quad \text{(C2)}$$

Calibration was conducted by collecting 10 000 traces, each with a duration of 50 ms. The average PSDs were then

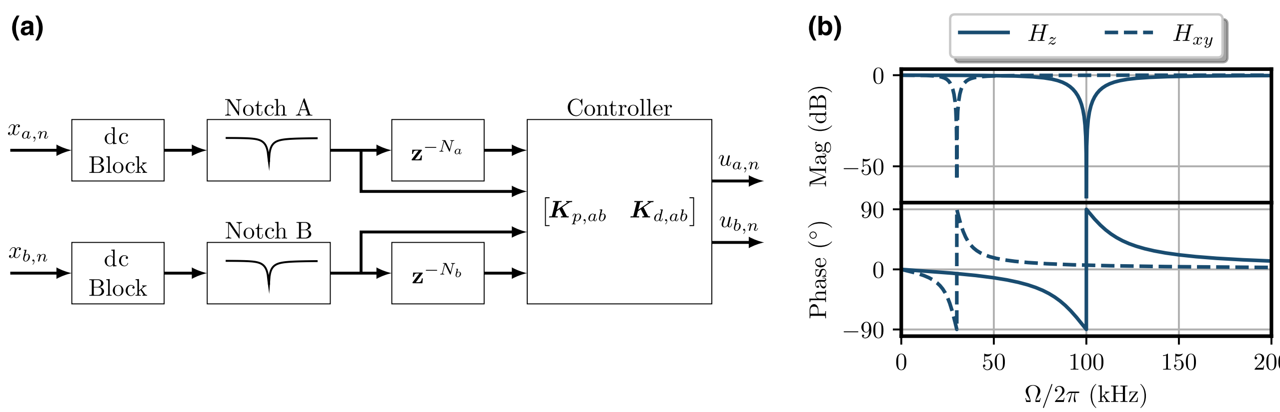

FIG. 5. Digital electronic implementation. (a) Block diagram illustrating the FPGA implementation for stable control of the particle's CoM motion. The digital filters are responsible for signal conditioning. A block random access memory allows the implementation of delay blocks, delaying the signal in multiples (N_a, N_b) of the sampling time. The delayed and nondelayed filtered signals are then transmitted to the controllers to compute the output signals. (b) Bode plots for each notch filter H_z and H_{xy}, depicting their magnitude and phase behavior for the frequency range of interest.

fitted to Eq. (C2), enabling the extraction of C^i_{Vm}, Ω_i, and γ_m. The coefficients were found to be

$$C^x_{Vm} = (6.87 \pm 0.72) \times 10^5\ \mathrm{V/m},$$
$$C^y_{Vm} = (7.08 \pm 0.75) \times 10^5\ \mathrm{V/m},$$
$$C^z_{Vm} = (1.07 \pm 0.11) \times 10^6\ \mathrm{V/m}.$$

Given these calibration factors, and considering a completely decoupled detection scheme, the **C** matrix can be expressed as

$$\mathbf{C} = \begin{bmatrix} C^x_{Vm} & 0 & 0 & 0 & 0 & 0 \\ 0 & C^y_{Vm} & 0 & 0 & 0 & 0 \\ 0 & 0 & C^z_{Vm} & 0 & 0 & 0 \end{bmatrix}. \qquad \text{(C3)}$$

2. Electrode calibration

To compute the controller's gain matrix $\mathbf{K}_d$, as described in Appendix A, it is necessary to measure the transduction coefficient C^{ij}_{NV} that provides the linear relation between the voltage applied across the electrodes j and the resulting force along the i axis. From these, it is possible to reconstruct the terms of the **B** matrix which, due to the geometry of the actuators, couples the x and y axes.

Force calibration of the electrodes can be carried out by measuring the particle's response to sinusoidal voltage drives applied to an individual pair of electrodes at known frequencies near each resonance [12]. The driving voltage in electrode j introduces a sinusoidal force $F^j_i \cos(\Omega_{dr} t)$, which can be observed within the PSD of the driven CoM motion of the i direction S^j_{ii},

$$S^j_{ii} = S_{ii}(\Omega) + S^{j,\mathrm{el}}_{ii}(\Omega), \qquad \text{(C4)}$$

where $S_{ii}(\Omega)$ follows Eq. (13) and $S^{j,\mathrm{el}}_{ii}(\Omega)$ is

$$S^{j,\mathrm{el}}_{ii}(\Omega) = \frac{{F^j_i}^2 \tau_{\mathrm{el}} \operatorname{sinc}^2[(\Omega - \Omega_{dr})\tau_{\mathrm{el}}]}{m^2[(\Omega^2 - \Omega_i^2)^2 + \gamma_m^2 \Omega^2]}, \qquad \text{(C5)}$$

with τ_{el} being the duration of the measurement.

In Fig. 6(a), the calibration curves for each coefficient are shown, yielding

$$C^{xx}_{NV} = (2.83 \pm 0.14) \times 10^{-16}\ \mathrm{N/V}$$
$$C^{xy}_{NV} = (2.18 \pm 0.13) \times 10^{-16}\ \mathrm{N/V}$$
$$C^{yx}_{NV} = (2.21 \pm 0.13) \times 10^{-16}\ \mathrm{N/V}$$
$$C^{yy}_{NV} = (2.36 \pm 0.12) \times 10^{-16}\ \mathrm{N/V}$$

An example of one of the PSDs used for calibration is presented in Fig. 6(b).

3. Gain matrix

After ensuring proper calibration of the detectors and actuators, computation of the LQR gains becomes feasible. Analysis of the x, y, and z PSDs confirms the trapped nanoparticle's oscillation frequencies $\Omega_x/2\pi = 96.24$ kHz, $\Omega_y/2\pi = 101.49$ kHz, and $\Omega_z/2\pi = 31.52$ kHz. Given the average diameter of the nanoparticle as provided by the manufacturer, its mass is

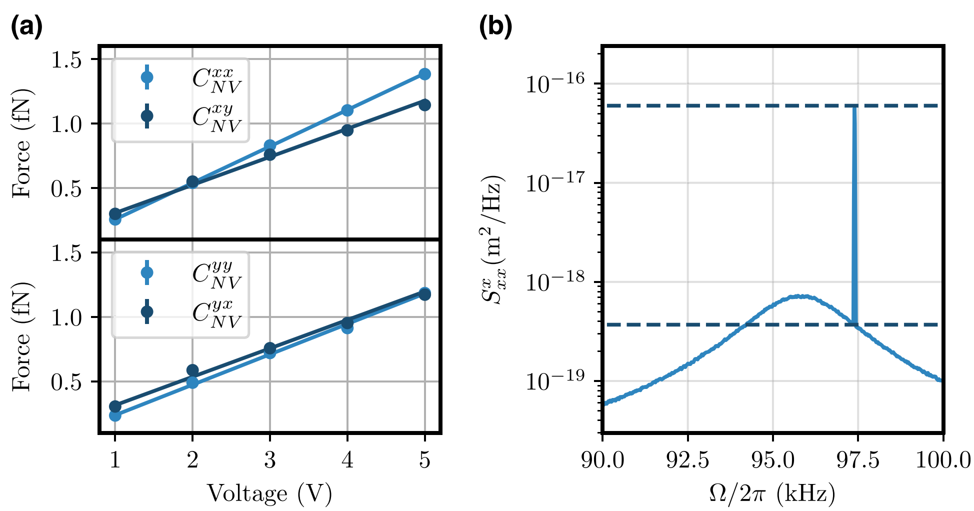

FIG. 6. Electrode calibration. (a) Calibration curves are presented for each coefficient of the xy plane. Each point corresponds to the analysis of 7000 traces with an individual duration of 50 ms. The particle was driven with a sinusoidal signal at $\Omega_{dr}/2\pi = 97.50$ kHz. (b) PSD of the particle's CoM motion under the action of a sinusoidal force. The dashed line delineates the peak region from which the amplitude of the force F_0 can be extracted.

calculated to be $m \approx 3.37$ fg. The weighting and cost-effort matrices used were

$$\mathbf{R}_d = m \begin{bmatrix} \mathrm{diag}(\Omega^2) & \mathbf{0}_{3\times 3} \\ \mathbf{0}_{3\times 3} & I_3 \end{bmatrix}, \tag{C6}$$

and

$$\mathbf{Q}_d = \frac{100}{m} \begin{bmatrix} \Omega_x^{-2} & 0 & 0 \\ 0 & \Omega_y^{-2} & 0 \\ 0 & 0 & \Omega_z^{-2} \end{bmatrix}. \tag{C7}$$

These matrices were selected to ensure that the cost function J_d possesses appropriate energy units, considering the states measured in SI units and $\mathbf{u}$ accounting for feedback forces. Such dimensional considerations are crucial for converting the controller's gain from the LQR theory to the digital gains configured in the FPGA. The $\mathbf{B}$ matrix is expressed as

$$\mathbf{B} = \begin{bmatrix} \mathbf{0}_{3\times 3} \\ \mathbf{B}_{xyz} \end{bmatrix}, \quad \text{where } \mathbf{B}_{xyz} = \begin{bmatrix} \mathbf{B}_{xy} & 0 \\ \mathbf{0}_{1\times 2} & b_z \end{bmatrix}. \tag{C8}$$

The submatrix $\mathbf{B}_{xy}$, expressed in kg^{-1}, is determined by m and the proportions of the electrode coefficients C_{NV}^{ij},

$$\mathbf{B}_{xy} = \frac{1}{m} \begin{bmatrix} -1 & C_{NV}^{xy}/C_{NV}^{xx} \\ C_{NV}^{yx}/C_{NV}^{xx} & C_{NV}^{yy}/C_{NV}^{xx} \end{bmatrix}. \tag{C9}$$

Without loss of generality, its terms were normalized by the largest transduction coefficient, C_{NV}^{xx}. The negative sign accounts for the orientation of the electrode axes, x' and y', as illustrated in Fig. 1.

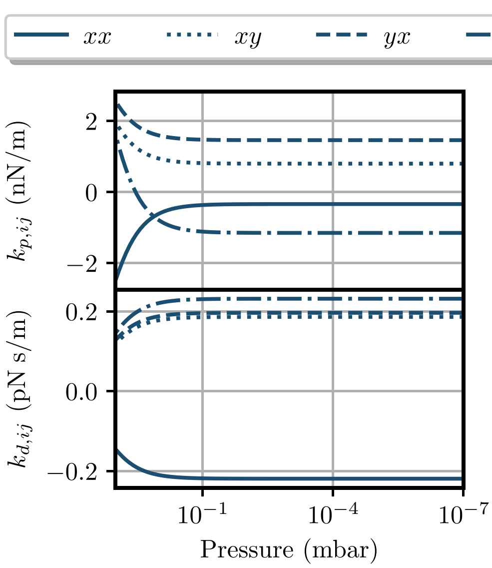

FIG. 7. Dependence of optimal gains on pressure. The constant behavior for values below 1 mbar allows one to employ the same matrix $\mathbf{K}_d$ for the underdamped and undamped regimes.

TABLE I. Controller gains. The values returned by optimal control theory and the values implemented within the FPGA are shown according to the system characterization and Eq. (C10). The digital gains had to pass through a conversion to a fixed-point representation during the VHDL implementation, allowing arithmetical operations with minimal loss of numerical resolution [65].

Gain	LQR [Eq. (A5)]	Digital Gains [Eq. (C10)]
$k_{p,xx}$	-3.40×10^{-10} N/m	−0.35
$k_{p,xy}$	7.99×10^{-10} N/m	0.80
$k_{p,yx}$	1.46×10^{-9} N/m	1.50
$k_{p,yy}$	-1.15×10^{-9} N/m	−1.15
$k_{d,xx}$	-2.19×10^{-13} N s/m	136.45
$k_{d,xy}$	1.86×10^{-13} N s/m	−119.14
$k_{d,yx}$	1.96×10^{-13} N s/m	−122.22
$k_{d,yy}$	2.32×10^{-13} N s/m	−148.23

The final parameter required to fully describe the dynamics given by Eq. (4) is γ_m. To assess the impact of varying this parameter, we substitute the values for the resonance frequencies, $\mathbf{B}$, T_s, $\mathbf{Q}_d$, and $\mathbf{R}_d$, and we compute $\mathbf{K}_d$ for different drag coefficients. The results of this evaluation are depicted in Fig. 7. Notably, for pressures below 1 mbar, the influence of γ_m on the controller's gains is negligible. Therefore, under the premise that pressure solely affects the drag coefficient, $\mathbf{K}_d$ can be computed only once, even as the pressure reduces.

After completing the system characterization, with γ_m considered as zero, $\mathbf{K}_d$ can be properly computed. The next step involves converting the theoretical gains into digital values configured within the FPGA. The following expressions govern this conversion

$$k_{p,ij}^d = \frac{k_{p,ij}}{A C_{NV}^{xx} C_{Vm}^j}, \tag{C10a}$$

$$k_{d,ij}^d = -\frac{\Omega_j k_{d,ij}}{A C_{NV}^{xx} C_{Vm}^j}. \tag{C10b}$$

Here, Ω_j emerges from estimating the velocity as being proportional to the delayed position, leading, for example, to $\dot{x} = -\Omega_x x(t - \tau_x)$, for a delay τ_x. The factor C_{NV}^{xx} arises from the $\mathbf{B}_{xy}$ matrix normalization, while C_{Vm}^j is used to convert displacement in the j axis to output voltages from its detector. In Table I, both theoretical and digital gains are presented.

[1] A. Ashkin, J. M. Dziedzic, J. E. Bjorkholm, and S. Chu, Observation of a single-beam gradient force optical trap for dielectric particles, Opt. Lett. **11**, 288 (1986).

[2] J. Millen, T. S. Monteiro, R. Pettit, and A. N. Vamivakas, Optomechanics with levitated particles, Rep. Progr. Phys. **83**, 026401 (2020).

[3] C. Gonzalez-Ballestero, M. Aspelmeyer, L. Novotny, R. Quidant, and O. Romero-Isart, Levitodynamics: Levitation and control of microscopic objects in vacuum, Science **374**, eabg3027 (2021).

[4] J. Gieseler, J. R. Gomez-Solano, A. Magazzù, I. P. Castillo, L. P. García, M. Gironella-Torrent, X. Viader-Godoy, F. Ritort, G. Pesce, A. V. Arzola, *et al.*, Optical tweezers—from calibration to applications: A tutorial, Adv. Opt. Photonics **13**, 74 (2021).

[5] W. Paul, Electromagnetic traps for charged and neutral particles, Rev. Mod. Phys. **62**, 531 (1990).

[6] D. Goldwater, B. A. Stickler, L. Martinetz, T. E. Northup, K. Hornberger, and J. Millen, Levitated electromechanics: All-electrical cooling of charged nano- and micro-particles, Quantum Sci. Technol. **4**, 024003 (2019).

[7] L. Dania, D. S. Bykov, M. Knoll, P. Mestres, and T. E. Northup, Optical and electrical feedback cooling of a silica nanoparticle levitated in a Paul trap, Phys. Rev. Res. **3**, 013018 (2021).

[8] D. S. Bykov, M. Meusburger, L. Dania, and T. E. Northup, Hybrid electro-optical trap for experiments with levitated particles in vacuum, Rev. Sci. Instrum. **93**, 073201 (2022).

[9] E. Bonvin, L. Devaud, M. Rossi, A. Militaru, L. Dania, D. S. Bykov, O. Romero-Isart, T. E. Northup, L. Novotny, and M. Frimmer, State expansion of a levitated nanoparticle in a dark harmonic potential, Phys. Rev. Lett. **132**, 253602 (2024).

[10] D. Hempston, J. Vovrosh, M. Toroš, G. Winstone, M. Rashid, and H. Ulbricht, Force sensing with an optically levitated charged nanoparticle, Appl. Phys. Lett. **111**, 133111 (2017).

[11] G. Ranjit, M. Cunningham, K. Casey, and A. A. Geraci, Zeptonewton force sensing with nanospheres in an optical lattice, Phys. Rev. A **93**, 053801 (2016).

[12] F. Ricci, M. T. Cuairan, G. P. Conangla, A. W. Schell, and R. Quidant, Accurate mass measurement of a levitated nanomechanical resonator for precision force-sensing, Nano Lett. **19**, 6711 (2019).

[13] J. Ahn, Z. Xu, J. Bang, P. Ju, X. Gao, and T. Li, Ultrasensitive torque detection with an optically levitated nanorotor, Nat. Nanotechnol. **15**, 89 (2020).

[14] C. Montoya, E. Alejandro, W. Eom, D. Grass, N. Clarisse, A. Witherspoon, and A. A. Geraci, Scanning force sensing at micrometer distances from a conductive surface with nanospheres in an optical lattice, Appl. Opt. **61**, 3486 (2022).

[15] U. Delić, M. Reisenbauer, K. Dare, D. Grass, V. Vuletić, N. Kiesel, and M. Aspelmeyer, Cooling of a levitated nanoparticle to the motional quantum ground state, Science **367**, 892 (2020).

[16] J. Piotrowski, D. Windey, J. Vijayan, C. Gonzalez-Ballestero, A. de los Ríos Sommer, N. Meyer, R. Quidant, O. Romero-Isart, R. Reimann, and L. Novotny, Simultaneous ground-state cooling of two mechanical modes of a levitated nanoparticle, Nat. Phys. **19**, 1009 (2023).

[17] L. Magrini, P. Rosenzweig, C. Bach, A. Deutschmann-Olek, S. G. Hofer, S. Hong, N. Kiesel, A. Kugi, and M. Aspelmeyer, Real-time optimal quantum control of mechanical motion at room temperature, Nature **595**, 373 (2021).

[18] F. Tebbenjohanns, M. L. Mattana, M. Rossi, M. Frimmer, and L. Novotny, Quantum control of a nanoparticle optically levitated in cryogenic free space, Nature **595**, 378 (2021).

[19] J. Rieser, M. A. Ciampini, H. Rudolph, N. Kiesel, K. Hornberger, B. A. Stickler, M. Aspelmeyer, and U. Delić, Tunable light-induced dipole-dipole interaction between optically levitated nanoparticles, Science **377**, 987 (2022).

[20] T. Penny, A. Pontin, and P. Barker, Sympathetic cooling and squeezing of two colevitated nanoparticles, Phys. Rev. Res. **5**, 013070 (2023).

[21] V. Liška, T. Zemánková, V. Svak, P. Jákl, J. Ježek, M. Bránecký, S. H. Simpson, P. Zemánek, and O. Brzobohatý, Cold damping of levitated optically coupled nanoparticles, Optica **10**, 1203 (2023).

[22] I. Brandão, D. Tandeitnik, and T. Guerreiro, Coherent scattering-mediated correlations between levitated nanospheres, Quantum Sci. Technol. **6**, 045013 (2021).

[23] J. Vijayan, J. Piotrowski, C. Gonzalez-Ballestero, K. Weber, O. Romero-Isart, and L. Novotny, Cavity-mediated long-range interactions in levitated optomechanics, Nat. Phys. **20**, 859 (2024).

[24] J. Gieseler and J. Millen, Levitated nanoparticles for microscopic thermodynamics—A review, Entropy **20**, 326 (2018).

[25] A. Dechant, N. Kiesel, and E. Lutz, All-optical nanomechanical heat engine, Phys. Rev. Lett. **114**, 183602 (2015).

[26] J. Millen and A. Xuereb, Perspective on quantum thermodynamics, New J. Phys. **18**, 011002 (2016).

[27] M. Debiossac, D. Grass, J. J. Alonso, E. Lutz, and N. Kiesel, Thermodynamics of continuous non-Markovian feedback control, Nat. Commun. **11**, 1360 (2020).

[28] M. Debiossac, M. L. Rosinberg, E. Lutz, and N. Kiesel, Non-Markovian feedback control and acausality: An experimental study, Phys. Rev. Lett. **128**, 200601 (2022).

[29] J. Gieseler, L. Novotny, and R. Quidant, Thermal nonlinearities in a nanomechanical oscillator, Nat. Phys. **9**, 806 (2013).

[30] F. Ricci, R. A. Rica, M. Spasenović, J. Gieseler, L. Rondin, L. Novotny, and R. Quidant, Optically levitated nanoparticle as a model system for stochastic bistable dynamics, Nat. Commun. **8**, 15141 (2017).

[31] O. Kremer, D. Tandeitnik, R. Mufato, I. Califrer, B. Calderoni, F. Calliari, B. Melo, G. Temporão, and T. Guerreiro, Perturbative nonlinear feedback forces for optical levitation experiments, Phys. Rev. A **109**, 023521 (2024).

[32] R. Muffato, T. Georgescu, J. Homans, T. Guerreiro, Q. Wu, D. Chisholm, M. Carlesso, M. Paternostro, and H. Ulbricht, Generation of classical non-Gaussian distributions by squeezing a thermal state into non-linear motion of levitated optomechanics, ArXiv:2401.04066.

[33] A. Arvanitaki and A. A. Geraci, Detecting high-frequency gravitational waves with optically levitated sensors, Phys. Rev. Lett. **110**, 071105 (2013).

[34] G. Afek, F. Monteiro, J. Wang, B. Siegel, S. Ghosh, and D. C. Moore, Limits on the abundance of millicharged particles bound to matter, Phys. Rev. D **104**, 012004 (2021).

[35] F. Monteiro, G. Afek, D. Carney, G. Krnjaic, J. Wang, and D. C. Moore, Search for composite dark matter with

optically levitated sensors, Phys. Rev. Lett. **125**, 181102 (2020).
[36] D. C. Moore and A. A. Geraci, Searching for new physics using optically levitated sensors, Quantum Sci. Technol. **6**, 014008 (2021).
[37] G. Afek, D. Carney, and D. C. Moore, Coherent scattering of low mass dark matter from optically trapped sensors, Phys. Rev. Lett. **128**, 101301 (2022).
[38] G. P. Winstone, D. H. Grass, A. Wang, S. Klomp, A. Laeuger, C. Galla, C. Montoya, N. Aggarwal, J. Sprague, A. Poverman, *et al.*, in *Optical and Quantum Sensing and Precision Metrology II* (SPIE, San Francisco, California, USA, 2022), Vol. 12016, p. 57.
[39] I. Pikovski, M. R. Vanner, M. Aspelmeyer, M. Kim, and Č. Brukner, Probing Planck-scale physics with quantum optics, Nat. Phys. **8**, 393 (2012).
[40] T. Weiss, M. Roda-Llordes, E. Torrontegui, M. Aspelmeyer, and O. Romero-Isart, Large quantum delocalization of a levitated nanoparticle using optimal control: Applications for force sensing and entangling via weak forces, Phys. Rev. Lett. **127**, 023601 (2021).
[41] L. Neumeier, M. A. Ciampini, O. Romero-Isart, M. Aspelmeyer, and N. Kiesel, Fast quantum interference of a nanoparticle via optical potential control, Proc. Natl. Acad. Sci. **121**, e2306953121 (2024).
[42] P. T. Grochowski, H. Pichler, C. A. Regal, and O. Romero-Isart, Quantum control of continuous systems via nonharmonic potential modulation, ArXiv:2311.16819.
[43] K. Aikawa and M. Kamba, Revealing the velocity uncertainties of a levitated particle in the quantum ground state, Phys. Rev. Lett. **131**, 183602 (2023).
[44] V. Jain, J. Gieseler, C. Moritz, C. Dellago, R. Quidant, and L. Novotny, Direct measurement of photon recoil from a levitated nanoparticle, Phys. Rev. Lett. **116**, 243601 (2016).
[45] L. Hackermüller, K. Hornberger, B. Brezger, A. Zeilinger, and M. Arndt, Decoherence of matter waves by thermal emission of radiation, Nature **427**, 711 (2004).
[46] G. P. Conangla, F. Ricci, M. T. Cuairan, A. W. Schell, N. Meyer, and R. Quidant, Optimal feedback cooling of a charged levitated nanoparticle with adaptive control, Phys. Rev. Lett. **122**, 223602 (2019).
[47] F. Tebbenjohanns, M. Frimmer, A. Militaru, V. Jain, and L. Novotny, Cold damping of an optically levitated nanoparticle to microkelvin temperatures, Phys. Rev. Lett. **122**, 223601 (2019).
[48] J. Gieseler, B. Deutsch, R. Quidant, and L. Novotny, Subkelvin parametric feedback cooling of a laser-trapped nanoparticle, Phys. Rev. Lett. **109**, 103603 (2012).
[49] M. Rosinberg, T. Munakata, and G. Tarjus, Stochastic thermodynamics of Langevin systems under time-delayed feedback control: Second-law-like inequalities, Phys. Rev. E **91**, 042114 (2015).
[50] F. Tebbenjohanns, M. Frimmer, and L. Novotny, Optimal position detection of a dipolar scatterer in a focused field, Phys. Rev. A **100**, 043821 (2019).
[51] V. Belavkin, in *Quantum communications and measurement* (Springer, Nottingham, United Kingdom, 1995), p. 381.
[52] V. Belavkin, Measurement, filtering and control in quantum open dynamical systems, Rep. Math. Phys. **43**, A405 (1999).
[53] H. M. Wiseman and G. J. Milburn, *Quantum Measurement and Control* (Cambridge University Press, Cambridge, United Kingdom, 2009).
[54] B. Melo, M. T. Cuairan, G. F. Tomassi, N. Meyer, and R. Quidant, Vacuum levitation and motion control on chip, Nat. Nanotechnol., 1 (2024).
[55] E. Bonvin, L. Devaud, M. Rossi, A. Militaru, L. Dania, D. S. Bykov, M. Teller, T. E. Northup, L. Novotny, and M. Frimmer, Hybrid Paul-optical trap with large optical access for levitated optomechanics, ArXiv:2312.10131.
[56] J. Gosling, A. Pontin, J. Iacoponi, P. Barker, and T. Monteiro, Sensing directional noise baths in levitated optomechanics, Phys. Rev. Res. **6**, 013129 (2024).
[57] G. F. Franklin, J. D. Powell, and A. Emami-Naeini, *Feedback Control of Dynamic Systems* (Pearson, London, 2015), Vol. 33.
[58] D. E. Kirk, *Optimal Control Theory: An Introduction* (Courier Corporation, New York, USA, 2004).
[59] R. E. Kalman, A new approach to linear filtering and prediction problems, J. Basic Eng. **82**, 35 (1960).
[60] K. J. Åström, *Introduction to Stochastic Control Theory* (Courier Corporation, New York, USA, 2012).
[61] F. Ricci, M. T. Cuairan, A. W. Schell, E. Hebestreit, R. A. Rica, N. Meyer, and R. Quidant, A chemical nanoreactor based on a levitated nanoparticle in vacuum, ACS Nano **16**, 8677 (2022).
[62] M. Frimmer, K. Luszcz, S. Ferreiro, V. Jain, E. Hebestreit, and L. Novotny, Controlling the net charge on a nanoparticle optically levitated in vacuum, Phys. Rev. A **95**, 061801 (2017).
[63] G. F. Franklin, J. D. Powell, and M. L. Workman, *Digital Control of Dynamic Systems* (Addison-wesley Menlo Park, CA, 1998), Vol. 3.
[64] E. Hebestreit, M. Frimmer, R. Reimann, C. Dellago, F. Ricci, and L. Novotny, Calibration and energy measurement of optically levitated nanoparticle sensors, Rev. Sci. Instrum. **89**, 00 (2018).
[65] P. Wilson, *Design Recipes for FPGAs* (Newnes, Oxford, United Kingdom, 2015).